

Synergistic improvement in bake-hardening response and natural aging stability of Al-Mg-Si-Cu-Zn alloys via non-isothermal pre-aging treatment

Li, Gaojie; Guo, Mingxing; Du, Jinqing; Zhuang, Linzhong

DOI

[10.1016/j.matdes.2022.110714](https://doi.org/10.1016/j.matdes.2022.110714)

Publication date

2022

Document Version

Final published version

Published in

Materials and Design

Citation (APA)

Li, G., Guo, M., Du, J., & Zhuang, L. (2022). Synergistic improvement in bake-hardening response and natural aging stability of Al-Mg-Si-Cu-Zn alloys via non-isothermal pre-aging treatment. *Materials and Design*, 218, Article 110714. <https://doi.org/10.1016/j.matdes.2022.110714>

Important note

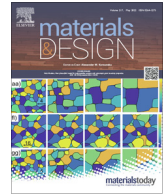
To cite this publication, please use the final published version (if applicable). Please check the document version above.

Copyright

Other than for strictly personal use, it is not permitted to download, forward or distribute the text or part of it, without the consent of the author(s) and/or copyright holder(s), unless the work is under an open content license such as Creative Commons.

Takedown policy

Please contact us and provide details if you believe this document breaches copyrights. We will remove access to the work immediately and investigate your claim.



Synergistic improvement in bake-hardening response and natural aging stability of Al-Mg-Si-Cu-Zn alloys via non-isothermal pre-aging treatment

Gaojie Li ^{a,c}, Mingxing Guo ^{a,b,*}, Jinqing Du ^a, Linzhong Zhuang ^{a,b}

^a State Key Laboratory for Advanced Metals and Materials, University of Science and Technology Beijing, Beijing 100083, China

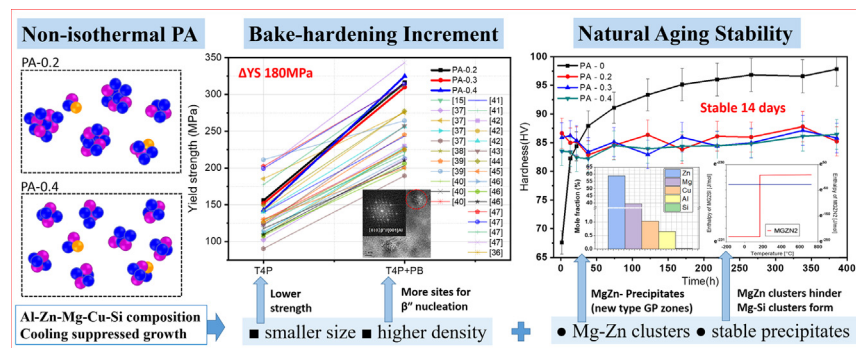
^b Beijing Laboratory of Metallic Materials and Processing for Modern Transportation, University of Science and Technology Beijing, Beijing 100083, China

^c Department of Materials Science and Engineering, Delft University of Technology, 2628 CD Delft, the Netherlands

HIGHLIGHTS

- Super-high bake hardening increment of 180 MPa can be achieved by non-isothermal pre-aging treatment.
- The microhardness of pre-aged alloys can remain unchanged up to 14 days during natural aging.
- Precipitation behavior of pre-aged alloys was deeply studied.
- The strengthening and natural stabilizing mechanisms of alloys were revealed in this paper.

GRAPHICAL ABSTRACT



ARTICLE INFO

Article history:

Received 18 February 2022

Revised 13 April 2022

Accepted 30 April 2022

Available online 4 May 2022

Keywords:

Non-isothermal pre-aging
Al-Mg-Si-Cu-Zn alloy
Bake hardening
GP zones

ABSTRACT

A new non-isothermal pre-aging treatment was proposed and utilized in Al-Mg-Si-Cu-Zn alloys, together with natural aging and artificial aging. The influence of cooling rates on subsequent precipitation behaviors was investigated by experimental and thermodynamic simulations. The results show that by controlling the formation of clusters/GP zones through changing pre-aging cooling rates, i.e. PA-0.2, PA-0.3 and PA-0.4 (°C/min, from 80 °C to 40 °C), an excellent bake hardening increment and natural aging stability can be obtained. The highest bake hardening increment can reach 180 MPa for PA-0.4 sample, which is twice higher than those of Al-Mg-Si-(Cu) alloys. The microhardness remains almost unchanged within NA for 14 days at a lower level of approximately 85 HV_{0.2}. Thermodynamic simulations estimate the solvus temperatures and chemical composition for GP zones, revealing the strengthening and stabilizing mechanisms behind: a) Mg-Zn- clusters formed during pre-aging can suppress Mg-Si- clusters formation in the natural aging process, b) non-isothermal hinders the precipitates growth, a faster cooling rate leads to smaller and softer Mg-Zn- clusters, and c) the formation of a heterogeneous microstructure contributes to the high bake-hardening response without changing the type of strengthening phase βⁿ. Finally, the clustering and aging process was illustrated and explained.

© 2022 The Author(s). Published by Elsevier Ltd. This is an open access article under the CC BY-NC-ND license (<http://creativecommons.org/licenses/by-nc-nd/4.0/>).

* Corresponding author at: State Key Laboratory for Advanced Metals and Materials, University of Science and Technology Beijing, Beijing 100083, China.

E-mail address: mingxingguo@skl.ustb.edu.cn (M. Guo).

1. Introduction

6xxx series Al-Mg-Si alloys have been used extensively in the automotive industry because they exhibit a high strength to

weight ratio, good formability and corrosion resistance, which can reduce the vehicle weight and lower the energy consumption and CO₂ emissions. However, even so, the strength is far from meeting the requirements compared with steels, which hampers its wide application. It is necessary to study the hardening mechanism and accordingly improve the hardening behaviours [1,2]. It is generally accepted that phase precipitation in Al-Mg-Si alloys occurs in the following sequence [3–7]:



where SSSS represents a supersaturated solid solution, clusters and GP zones are precipitates that are fully coherent with the matrix, and β'' is the main strengthening phase in Al alloys, which is expected to form during the bake-hardening process. β' represents metastable rod-like precipitates, and β is the equilibrium phase Mg₂Si. After involving Cu, the Q' phase was detected in the same state as β' . Normally, Al alloys are stored at room temperature (natural aging) for some time before being stamped into a final shape, during which precipitates inevitably form and cause the hardness to increase. Therefore, the formability is damaged, and the bake hardening response is also affected due to natural aging precipitation. Improving the strength in the use state while maintaining good formability before stamping is a trade-off for the wide application of Al alloys [2].

Preaging treatment is a promising method to avoid hardening precipitates during storage time, which is a thermal treatment that brings solution-treated samples immediately to a temperature that is higher than RT and holds for a certain time [8]. During the preaging process, clusters and GP zones precipitate from the metastable SSSS. On the one hand, the quenched vacancies are captured by solutes to form clusters, and the 'stable clusters' are more stable than SSSS during subsequent natural aging, hence inhibiting unexpected strengthening phenomena. On the other hand, 'stable clusters' act as nucleation sites for the β'' phase during the artificial aging process and accordingly accelerate the bake hardening response.

The preaging treatment was proven to be workable under appropriate heat treatment parameters [9]. Lizi He et al. [10] performed a preaging treatment from RT (20 °C) to 140 °C and found that the type of precipitates depended on PA conditions, and a positive effect occurred at PA over 80 °C. Chin-Hui Shen [11] combined preaging at 70 °C and pre-straining 2% and successfully improved the bake-hardening response in a natural aged alloy. Hengcheng Liao et al. [12] studied high-temperature preaging at 120 °C and detected the formation of β'' phases, which weakened the hardening response. Lizhen Yan et al. [13] observed clusters in 140 °C PA samples via 3DAP and proved that it is relevant to the β'' phase. Furthermore, preaging at higher temperatures (170 °C to 210 °C) has also been considered [14], aiming to overcome the negative effect of natural aging. Recent research performed a new kind of coil-cooling preaging treatment in Al-Mg-Si alloys and revealed the importance of Mg-Si co-clusters formed during the preaging step [15]. Some studies have also focused on solution treatment with quenching processes and found that the quenching rate influences quenching precipitation and subsequent precipitation evolution; therefore, the final mechanical properties can be improved by appropriate rate control [16]. Based on these findings, pre-aging treatment is essential for controlling clusters and affecting later precipitating behaviours. The non-isothermal pre-aging treatment in [15] also explained better the clustering process and excellent tensile test results in Al – Mg – Si alloy. However, the non-isothermal pre-aging treatment itself haven't been paid enough attention to understand the clustering and connect with following precipitating process.

Almost all the performed studies were to optimize the heat treatment parameters to adjust the preforming precipitates and

characterise following precipitation behaviours, i.e., study the preaging process in an indirect way. However, no study has focused on the preaging process itself. This is because the clusters, GP zones, and even β'' and β' phases, as metastable structures, are difficult to detect and quantify, especially for clusters and GP zones in the PA process, which do not have certain structures and compositions. Thus, there are very limited studies choosing to estimate the solvus temperature of metastable phases, especially GP zones, in a direct way in Al alloys. β'' phase simulation was performed by several studies [17–20], but GP zone simulation was mostly performed in Al-Cu-X series alloys [21–24].

Currently, studies are also trying to improve performance by widening Al-Mg-Si elemental systems [25–34], Zn addition [25–28] has proven to be effective in improving bake hardening response due to its high solubility in the Al matrix. The studies found Zn-containing solute clusters/GP zones based on the atom probe tomography characterisation, but there was no evidence of forming Mg-Zn phases even with high Zn content of 4.0 wt.% percent [27]. The reason for this phenomenon and how the Zn behaves at different aging process, are still unknown.

In the present study, we performed a new non-isothermal preaging treatment in Al-Mg-Si-Cu-3.0 wt%Zn alloy, aiming to affect the formation of multi-scale and multi-type clusters/GP zones by controlling the cooling rate within a specific temperature range, and also explore the behaviours of Zn element by chemical composition analysis of precipitates. By characterizing the microstructure and the following hardening effect, we are able to investigate their influence on subsequent precipitation behaviours during both natural aging and high temperature aging processes, both in experimental and modelling aspects.

2. Materials and experimental methods

The chemical composition of the experimental alloy is listed in Table 1. The raw materials were melted in a graphite crucible in an electrical resistance furnace (SG2-12-10) and then cast into an ingot in a steel mold.

After hot rolling, homogenization and first cold rolling, a 3 mm thick plate was obtained and subjected to an intermediate annealing process at 400 °C for 2.5 hrs to soften the material, which was followed by final cold rolling to obtain a 1 mm thick plate.

The plate was divided into four parts. After solution treatment at 555 °C for 2 min, the plate was subjected to different non-isothermal preaging treatments at rates of 0.2 °C/min, 0.3 °C/min, and 0.4 °C/min from 80 °C cooling to 40 °C. PA samples were marked as PA-0.2, PA-0.3, and PA-0.4. The solid solution-treated specimen PA-0 represents the specimen that was not subjected to the preaging treatment.

Vickers hardness measurements were performed under a load of 200 g and holding time of 15 s using a Wolpert-402 MVD micro-hardness tester. Each value was obtained by averaging at least seven indentations. Tensile tests were conducted with an Instron tensile testing machine after the specimens were thermomechanical treated, and a gauge length of 60 mm was utilized. Meanwhile, the precipitation behavior was analysed by differential scanning calorimetry (DSC) using QS2000 under an argon atmosphere with pure aluminum as a reference. The DSC test was carried out from room temperature (20 °C) to 370 °C at a heating rate of 10 °C/min. Transmission electron microscopy (TEM) images of precipitates were obtained using a Tecanai G2 F20 S-TWIN operated at an acceleration voltage of 200 kV. The specimen was prepared by standard mechanical grinding to a thickness of ~80 μm and then subjected to twin-jet electropolishing at –20 °C in a mixture solution with 30% HNO₃ and 70% CH₃OH. High-resolution TEM (HRTEM) characterization was performed along the [001]_{Al} direc-

Table 1
Chemical composition of experimental alloy (wt.%).

Alloy	Zn	Mg	Si	Cu	Mn	Fe	Al
L	3.0	0.9	0.7	0.2	0.3	≤0.4	Bal.

tion. The TEM results were analysed using Digital Micrograph software released by Gatan. The precipitates were confirmed by directly comparing to standard crystal structures created by CrystalMaker. Thermodynamic calculations were performed with Thermo-Calc 2021a using the TTAL7 and MALDEMO databases (see Fig. 1).

3. Results

3.1. Age hardening behavior

Fig. 2 shows the changes in the microhardness of samples PA-0, PA-0.2, PA-0.3 and PA-0.4 during the NA process. After heat treatment and NA for within 20 h, PA-0 sample has much lower hardness than PA samples, but it arises rapidly from 68HV to 90HV and reach almost the same hardness value with PA samples; From NA 20 h and forwards, the hardness of PA-0 exceeds PA samples and continues to rise during the following natural aging of thousands hours. Meanwhile, the hardness of the PA samples remains basically stable at approximately 83–85 HV. Within the NA treatment of 400 h (approximately 17 days), the hardness of the PA samples remains unchanged. After the NA of 500 h, the hardness begins to rise slowly but it was far lower than that of the PA-0 sample. After the NA of 3000 h (approximately 4 months), the hardness of the PA samples increases to 100 HV, reaching the same growth rate as that of the PA-0 sample. The difference in hardness between the PA-0 and PA samples gradually decreases after NA of 5000 h (approximately 7 months).

Among PA samples, there was no significant difference within the NA of 400 h. However, when NA time is over 400 h, there is a slight difference can be seen: the PA-0.2 sample maintains a lower hardness value during the slow hardness increasing process. This means that among the three pre-aging processes, PA-0.2 is beneficial to the inhibition of the formation and growth of precipitates, which displays better NA stabilization.

To meet the strength requirement, stamped alloys usually require a bake-hardening treatment, which can accelerate the precipitation of hard phase β'' in a short time; accordingly, the strength is improved. To understand the effect of PA on bake-hardening response, samples after NA for 0 days, 2 months, and 6 months are pre-strained 2% and then artificial aged at 185 °C, simulated bake-hardening treatment, to observe the changes in

micro hardness. The corresponding hardness curves are shown in Fig. 3 below.

For the samples with a NA after 0 days, as shown in Fig. 3(a), the hardness value fluctuates significantly during the artificial aging process. The PA-0.4 sample exhibits the highest hardness value, while the PA-0.3 and PA-0.2 samples are lower and fluctuate in a higher range, making the peak value not notable. The peak value appears at 150 min, with PA-0.4 the highest of 125HV, PA-0.2 the lower, and the PA-0.3 the lowest of only 120HV. The hardness change can be roughly divided into third stages. The first stage is the overall increase of hardness within 200 min, from beginning to the peak value of 125HV; the second stage is the period from 250 min to 850 min, the hardness value remains basically unchanged, maintaining at approximately 120HV; the last stage is after 850 min, the hardness value starts to decrease significantly after the plateau period.

For sample after NA of 2 months, as shown in Fig. 3(b), three PA samples do not show an effect on the hardness change. In the early stage of aging, the hardness values are lower than that of NA 0 days, indicating that after two months of NA, some unstable solute clusters in the alloy matrix redissolve. The hardness of PA-0.2 is the lowest, but it quickly rises to a level similar to that of the other two processes, indicating that the ageing response rate of PA-0.2 is the fastest. The peak hardness appears after 200 min, at approximately 125 HV, and there is no significant difference in the peak value among the three PA samples.

For sample after NA of 6 months, as shown in Fig. 3(c), at the early stage of aging, within 50 min, the hardness decreases significantly, indicating that the precipitated phase is redissolved in the matrix and then continues to precipitate and grow during the subsequent aging process to make the hardness rise and reach the hardness peak. As the aging time increases, the strengthening phase grows and transforms from the β'' phase to the β' and Q' phases, resulting in a decrease in hardness. Compared with the peak hardness of NA 2 months, the peak hardness after 6 months of NA has a significant decrease, and the peak also appears after 200 min. After the peak hardness time, the hardness value of PA-0.4 decreases most significantly, while PA-0.2 and PA-0.3 show better aging stability.

The three PA samples have similar harness tendencies at the same NA state. With the extension of the artificial aging time, the hardness first increases to the peak and then begins to decrease after reaching the peak. However, with the extension of the NA time, there are obvious differences: before the increasing trend, there is a slight decrease at the beginning of artificial aging process, as shown in the insert enlarge curves, the decrease is found within first 5 min for NA 2 months-artificial aging samples, ranging from 105HV to 100HV, while the decrease is found to occur within first 40 min for NA 6 months-artificial aging samples, ranging from 110HV to 95HV. This trend was not observed for the NA 0 day artificial aging samples.

This is mainly because a large number of dislocations are induced by 2% pre-strain deformation. During the artificial aging process of the NA 0 day samples, some Mg, Si, Zn atoms can quickly move through the dislocation channel, thereby accelerating the rapid precipitation of the strengthening phase, so the hardness values of Fig. 3(a) are the highest. After a long-term NA of 2 months or 6 months, the precipitated clusters and GP zones increase; with the increase in artificial aging time, these clusters and GP zones redis-

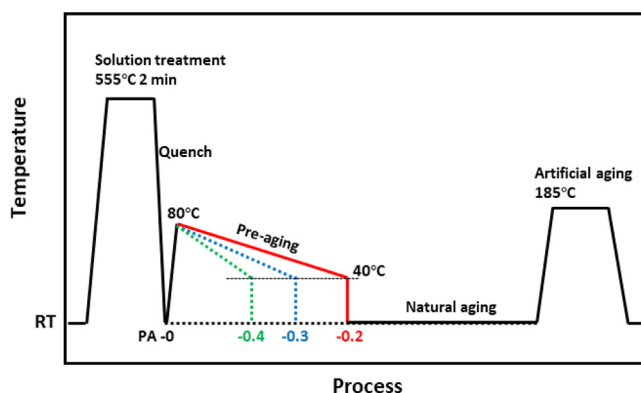


Fig. 1. Heat treatment process of studied alloy.

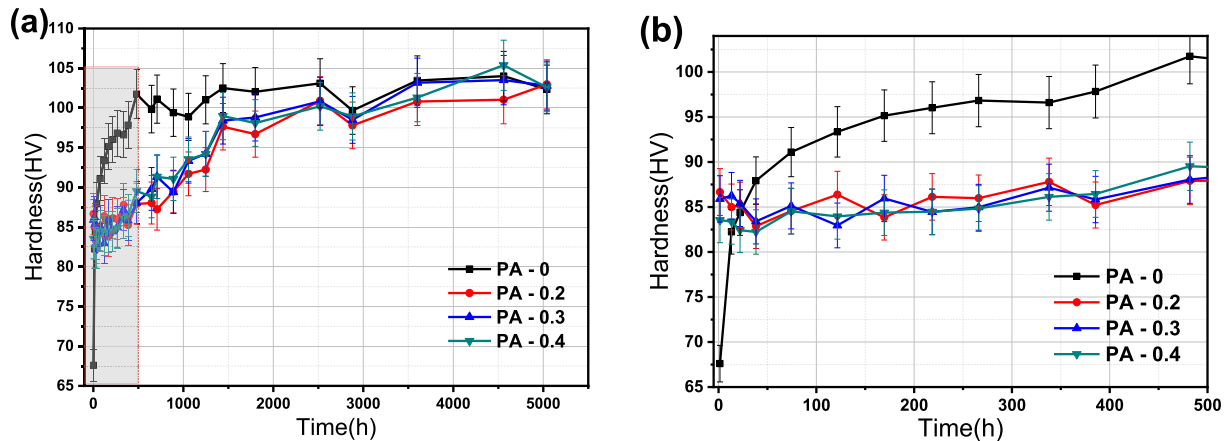


Fig. 2. Microhardness changes of samples PA-0, PA-0.2, PA-0.3, and PA-0.4 during the 6-month natural aging process (a) Natural aging for 6 months; (b) Zooming in the first 15 days of natural aging.

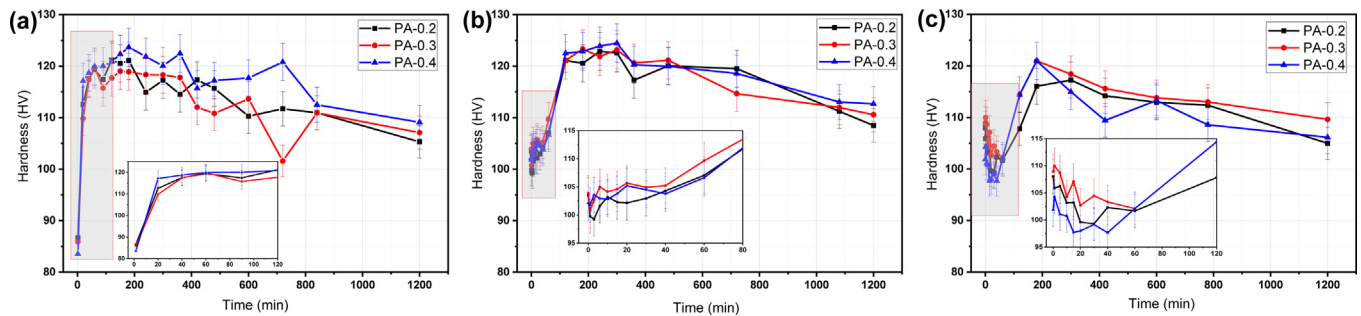


Fig. 3. Microhardness changes during 185 °C artificial aging of samples: (a) PA + PS 2% + 185 aging; (b) PA + NA 2 months + PS 2% + 185 aging; (c) PA + NA 6 months + PS 2% + 185 aging.

solve. At the same time, the dislocations introduced by pre-strain are consumed by recovery at the beginning of artificial aging. The joint effect causes the hardness to decrease, and the longer the NA time is, the more significantly the hardness value of aging decreases. With the extension of the aging time, the β'' strengthening phase is continuously precipitated, resulting in the alloy hardness rising again.

3.2. Mechanical property characterization

To directly evaluate the hardening response and mechanical properties, tensile tests were performed on samples that were PA treated and then NA for different times (marked as the T4P state). Similar to the hardness measurement, simulated paint baking treatments of 2% pre-strain and artificial aged for 20 min at 185 °C were also added to each T4P state (marked as the T4P + PB state). In the T4P state, the yield strength (YS) and elongation are recorded to evaluate the formability, while after baking in the T4P + PB state, the new yield strength (YS) allows us to calculate the hardness increment and reveal the hardening response. The testing results are shown in Table 2 and Fig. 4 below.

Table 2 shows that during the 6-month NA process, the YS in the T4P state tends to decrease and that in the T4P + PB state tends to increase, leading to a gradual drop in the YS increment. The highest bake hardening increment was found in the shortest NA samples. PA-0.2 and PA-0.3 show an increment of approximately 160 MPa, but PA-0.4 shows the highest 180 MPa, which comes from a 10 MPa lower YS in the T4P state and a 10 MPa higher YS in the T4P + PB state compared with the other 2 samples. The bake hardening increment is twice higher than those of traditional Al-

Mg-Si-Cu alloys (such as AA6016, AA6022) [15,35,36]. With NA time lasting, the increment of three samples gradually decreased and approached. After NA 2 months, the increment dropped below 100 MPa at around 70 ± 10 MPa, and after NA 6 months, the increment for three samples became almost the same at around 60 MPa, but the yield strengths of the alloys in the T4P + BH still can reach about 270 MPa.

Fig. 4 shows a more visible tendency of the YS increment during the long NA process. After NA 2 months, PA-0.2 shows a better bake hardening property. PA-0.4 decreased the fastest and PA-0.2 decreased the slowest, corresponding to the microhardness change tendency in the artificial aging state. Compared with relative studies in references as shown in Fig. 4 (b), which summarised all paint baking response of 6xxx series alloys up to date [36–47]. Apparently, the data line from references are more or less parallel to each other, indicating a similar YS increment. For YS at T4P state mostly lower than 150 MPa, the maximum YS at T4P + PB can reach 275 MPa, the best YS increment was observed in Ref. [47], from around 200 MPa to 340 MPa, leaving a 140 MPa hardenability than all the other research. However, our PA samples exhibit excellent hardening response that can reach 325 MPa at T4P + PB state while keeping the low YS at T4P state of only 150 MPa, combining the formability and hardenability successfully.

3.3. Precipitation kinetics analysis

Differential scanning calorimetry (DSC) is employed to study the effect of different PA treatments on precipitation behavior, which is an effective method for non-isothermal characterization. For the kinetic problems related to phase transformation and pre-

Table 2
Mechanical properties of PA samples in the T4P and T4P + PB states.

Processing	Sample	T4P state		T4P + PB state		Δ YS (MPa)
		YS (MPa)	Elongation %	YS (MPa)	UTS (MPa)	
NA < 1 day	PA-0.2	155.9	27.1	316.2	376.7	160.3
	PA-0.3	152.2	23.2	310.0	368.2	157.8
	PA-0.4	143.2	23.9	325.1	369.4	181.9
NA 2 months	PA-0.2	187.8	23.6	267.6	345.8	79.8
	PA-0.3	181.2	23.7	249.0	343.1	67.8
	PA-0.4	186.3	22.4	255.8	340.1	69.5
NA 6 months	PA-0.2	212.0	20.0	269.2	349.5	57.2
	PA-0.3	212.3	20.5	272.2	350.2	59.9
	PA-0.4	211.9	18.2	270.9	349.0	59.0

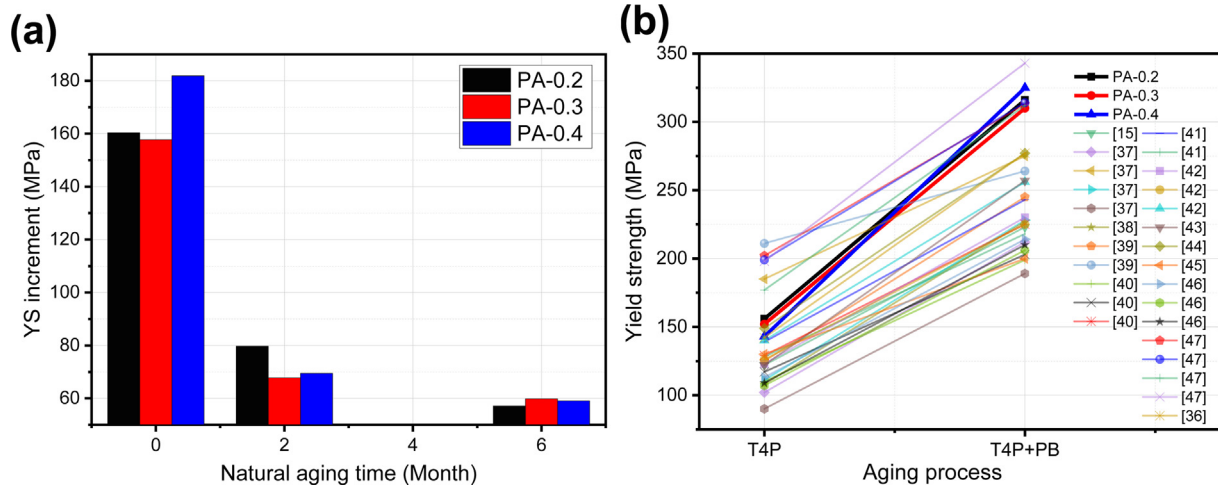


Fig. 4. Tensile test results of samples during long-term natural aging: (a) YS increment of PA samples; (b) comparable results from previous studies in all relating 6xxx series alloys (focus only on final paint baking response without considering optimizing methods like chemical composition or heat treatments).

precipitation during the preaging process, the Avrami-Johnson-Mehl equation is usually utilized [48,49]. We use the same calculation procedures to identify the activation energy Q and constant k_0 based on experimental results.

To study the influences of the PA and NA processes on the precipitation behaviour of alloys, the samples with different PA treatments and NA for 0 days and 6 months were subjected to DSC tests. The testing temperature rises from 20 °C to 380 °C with a heating rate of 10 °C/min. The test results are shown in Fig. 5.

Fig. 5(a) shows that there are two obvious peaks, which are at approximately 240 °C and 280 °C. There is also a small peak, which

is before 150 °C. The exothermic peak at approximately 240 °C corresponds to the precipitation of the β'' phase; the exothermic peak at approximately 280 °C corresponds to the precipitation of the β' and Q' phases [13]. For PA samples with different treatments, the three cooling preaging processes had no significant difference in the phase transition temperature of the β'' phase. The peak areas of the PA-0.2 and PA-0.3 samples are larger than that of the PA-0.4 sample. In detail, the PA-0.2 sample exhibits a higher β'' phase precipitation peak at approximately 240 °C and possesses a larger area, indicating that PA-0.2 can increase the amount of β'' phase precipitation.

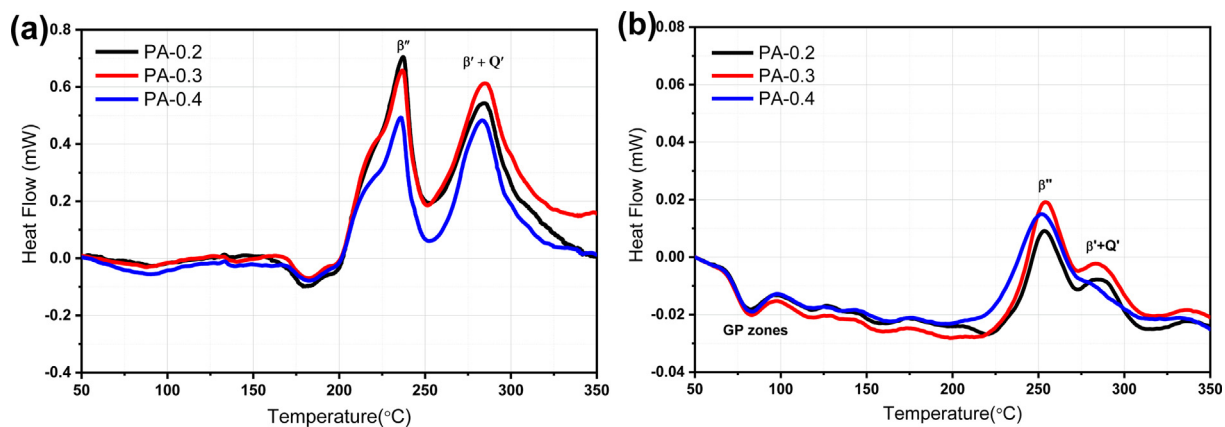


Fig. 5. DSC experimental results of PA samples after NA for (a) 0 days and (b) 6 months.

The test results in Fig. 5(b) show that the samples have a small endothermic peak at approximately 80 °C, two large exothermic peaks at approximately 250 °C and 280 °C, and one small exothermic peak at approximately 340 °C. The redissolution peaks appearing at approximately 80 °C are redissolution of the GP zone and Mg-Si clusters that precipitated during the NA process. The PA-0.2 sample has the narrowest redissolution peak and the smallest area, indicating that the PA-0.2 sample has the least clusters and the most stable performance during the natural aging process. However, comparing the peak areas of β'' precipitation and β' and Q' formation, the PA-0.2 sample shows the lowest fraction of β'' phase, resulting in the lowest peak-aging hardness compared to the other two samples.

Fig. 6(a) shows that the β'' phase precipitation of PA-0.2 occurs slightly earlier than that of the other two samples, indicating that this treatment reduces the phase transition point, which is conducive to the precipitation of the β'' phase. The precipitating end temperature is also higher, indicating that there is a longer time for β'' phase precipitation compared with the other two processes. This corresponds to the largest precipitation peak area in the DSC curve. Although PA-0.4 is always on the top of the other two lines, the later starting point and earlier ending point make the precipitation time of the β'' phase shorter, causing a lower fraction of the β'' phase. This is because in the previous cooling preaging process, the PA-0.2 sample has a slow cooling rate and a long aging time, during which more precipitated or grown clusters or GP regions are formed. There are more nucleation sites for the β'' phase at the early stage of precipitation, so the total volume of β'' is greater. For the PA-0.4 sample, the phase precipitation rate is faster, but the

total number of nucleation sites is limited, resulting in the lowest precipitation fraction of the β'' phase.

Fig. 6(b) shows that the slopes of the three curves are similar, which is calibrated $n = 2$ after linear fitting. The parameter n in the Avrami-Johnson-Mehl equation is set to 2. Then, we get Fig. 6(c). The calculated activation energies for β'' phase precipitation of the three PA samples are PA-0.4 > PA-0.3 > PA-0.2, which are 21.5 kJ/mol, 20.0 kJ/mol, and 19.9 kJ/mol, respectively, all approximately 20.0 kJ/mol. The lower the activation energy is, the easier the β'' phase precipitates. Therefore, among the three PA treatments, no significant difference was found, but the slowest cooling pre-aging treatment PA-0.2 slightly improved the bake hardening response.

Substituting the activation energy of β'' phase precipitation and the constant k_0 , the kinetic equation of β'' phase precipitation can be obtained, as shown in Table 3.

Similar to the previous analysis, Avrami-Johnson-Mehl is utilized to calculate the activation energy of β'' and precipitation kinetics, and the calculation results are shown in Fig. 7.

Fig. 7(a) shows the volume fraction Y of the β'' phase precipitated with temperature T . Apparently, the PA-0.3 sample is the earliest to precipitate, PA-0.2 is the latest and the reaction time is the shortest, and PA-0.4 is in the middle but with the longest precipitation time. PA-0.2 sample contains the least fraction of β'' phase. This is because in the early cooling preaging process, the PA-0.2 sample has more clusters or GP zones, which are relatively stable during 6 months of NA. However, in the PA-0.4 sample, clusters and GP zones are relatively small after PA, so they are unstable during the NA process. More GP zones are formed, which provides a

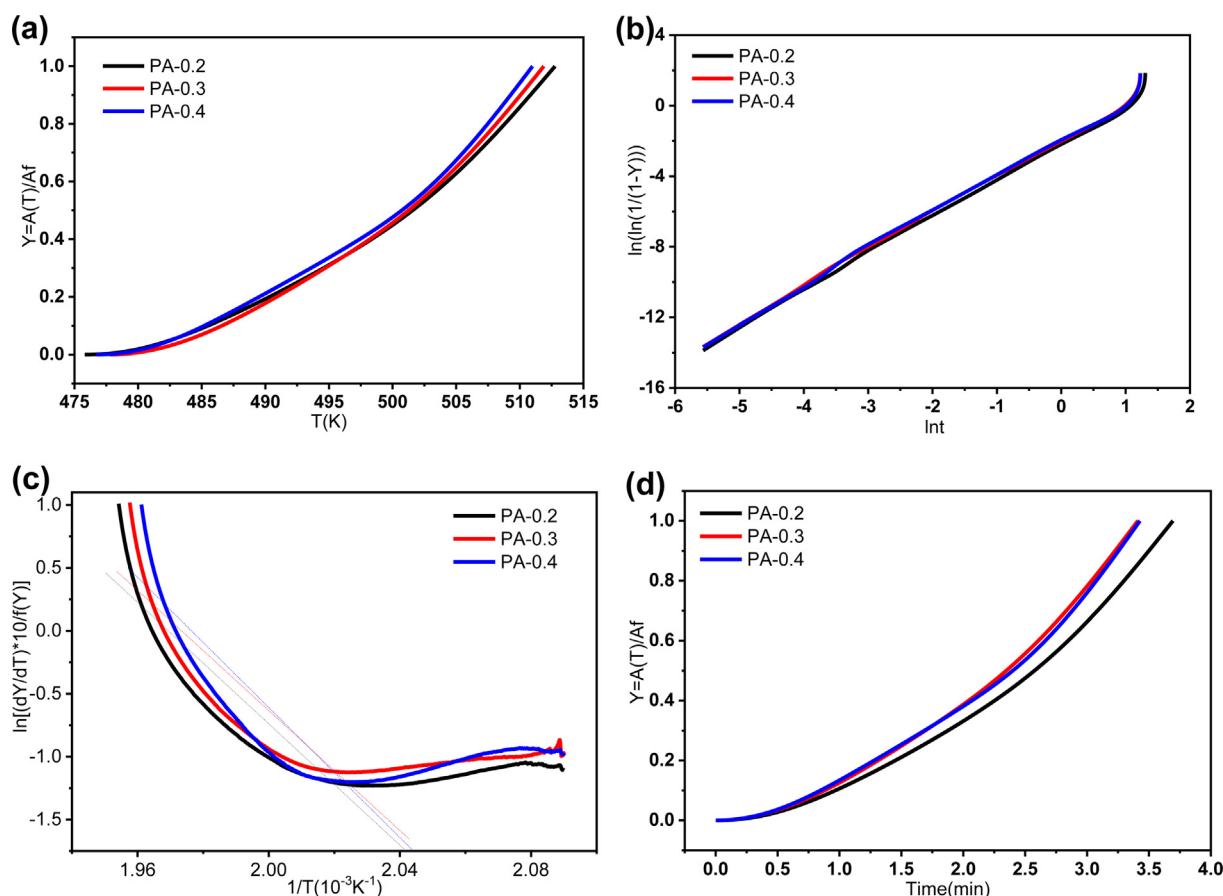


Fig. 6. Calculation procedure of β'' phase activation energy for PA-0.2, PA-0.3 and PA-0.4 after preaging treatments (a) Y-T curves of β'' phase fraction with temperature, (b) $\ln(\ln(1/(1-Y)))$ - $\ln t$ curves for n fitting, (c) $[(dY/dT) \cdot 10^6 / f(Y)]$ - $1/T$ curves for calculation slope Q , (d) Y-t curves of β'' phase fraction versus time.

Table 3
Activation Energy and Kinetics Equation of β'' after PA treatments and NA for 0 days.

Sample	Q (KJ/mol)	k_0 (min^{-1})	Kinetics Equation
PA-0.2	19.9	2.71×10^{20}	$Y = 1 - \exp[-(2.71 \times 10^{20} \exp(-23.84/T)t)^2]$
PA-0.3	20.0	4.22×10^{20}	$Y = 1 - \exp[-(4.22 \times 10^{20} \exp(-24.12/T)t)^2]$
PA-0.4	21.5	1.51×10^{22}	$Y = 1 - \exp[-(1.51 \times 10^{22} \exp(-25.84/T)t)^2]$

large number of precipitation sites for the subsequent β'' phase. As a result, in the PA-0.4 sample, the volume fraction of the β'' phase precipitated during the DSC heating process of the alloy exceeds that of the other two alloys.

Fig. 7(b) shows that the slopes of the curves are approximate, which is approximately 2 after linear fitting; the obtained $n = 2$ is brought into Fig. 7(c). The calculated activation energies of β'' phase precipitation in the three PA samples are PA-0.3 > PA-0.2 > PA-0.4, which are 33.3 kJ/mol, 31.8 kJ/mol and 19.7 kJ/mol, respectively. In other words, the PA-0.4 sample precipitates most of the β'' phase, and PA-0.2 and PA-0.3 are more or less the same. This is consistent with the hardness change during artificial aging at 185 °C.

From the previous calculation, the kinetic equation of β'' phase precipitation can be obtained, as shown in Table 4.

In summary, among the three cooling PA processes, the slowest cooling rate, i.e., The PA-0.2 sample shows better ageing hardening ability and promotes β'' precipitation after NA 0 days; although after NA 6 months, its ageing hardening ability is not as good as

Table 4
Activation Energy and Kinetics Equation of β'' after PA treatments and NA for 6 months.

Sample	Q (KJ/mol)	k_0 (min^{-1})	Kinetics Equation
PA-0.2	31.8	1.03×10^{32}	$Y = 1 - \exp[-(1.03 \times 10^{32} \exp(-38.24/T)t)^2]$
PA-0.3	33.3	2.74×10^{34}	$Y = 1 - \exp[-(2.74 \times 10^{34} \exp(-40.10/T)t)^2]$
PA-0.4	19.7	7.45×10^{19}	$Y = 1 - \exp[-(7.45 \times 10^{19} \exp(-23.70/T)t)^2]$

that of the other two pre-ageing treatment samples, taking into account its excellent natural ageing stability, the PA-0.2 sample is the most beneficial for improving alloy properties.

According to the above analysis, the PA-0.2 sample shows the best NA stability during NA 6 months, good bake hardening response during artificial aging, and a better softening resistance at the over peak aging state. It is necessary to evaluate the precipitation in the corresponding state to determine the underlying hardness changes.

For comparison, PA-0.2 samples after NA for 0 days and 6 months and artificial aged before peak aging, at peak aging, and over peak aging states are selected for TEM characterization. As shown in Figs. 8 and 9, samples were pre-strained to 2% and artificially aged at 185 °C for 20 min, 150 min and 20 hrs for PA-0.2NA 0 days state, and 185 °C for 20 min, 180 min and 20 hrs for PA-0.2NA 6 months state, respectively. High-resolution TEM images, together with fast Fourier transform (FFT) and corresponding diffraction spot simulation, are displayed below. Due to the

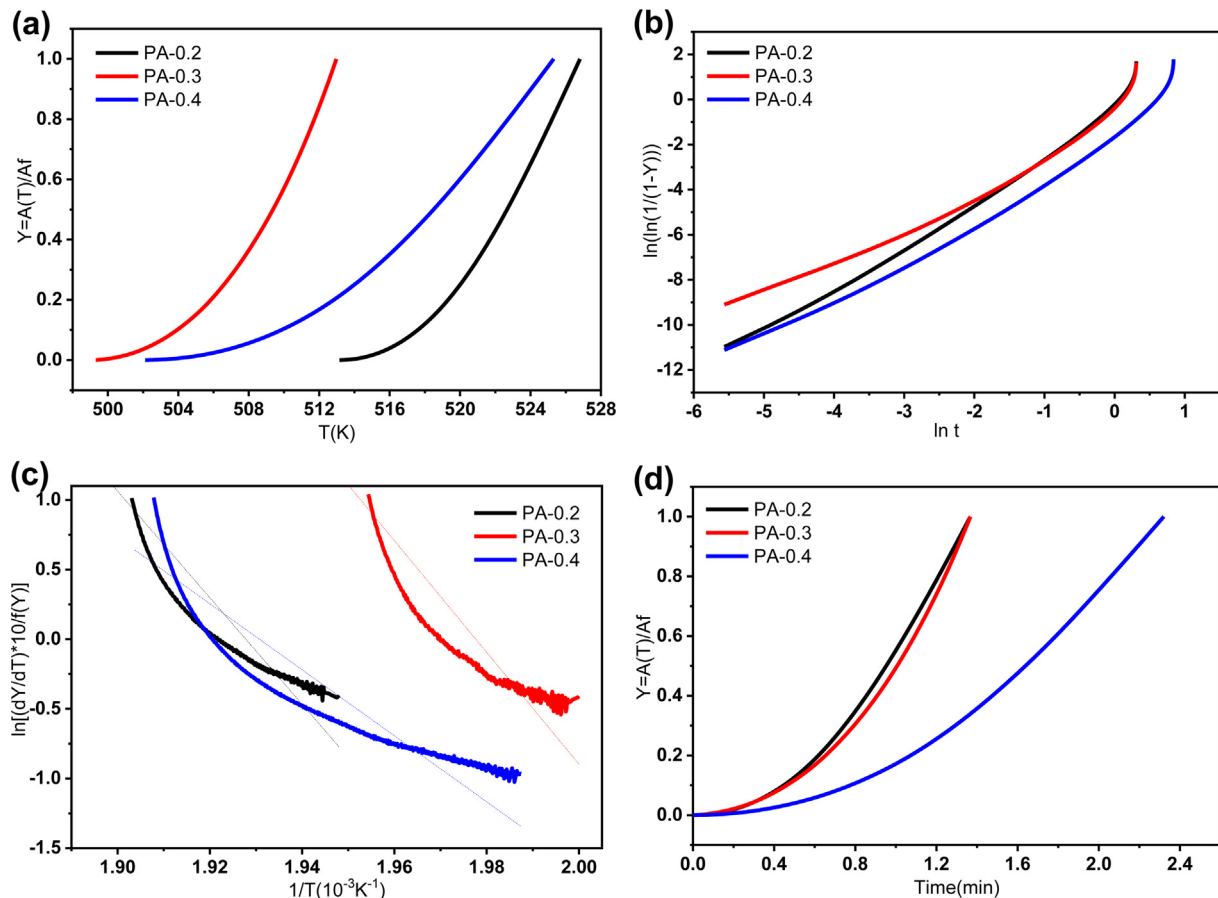


Fig. 7. Calculation procedure of β'' phase activation energy for PA-0.2, PA-0.3 and PA-0.4 after preaging treatments and NA for 6 months (a) Y-T curves of β'' phase fraction with temperature, (b) $\ln(\ln(1/(1 - Y))) - \ln t$ curves for n fitting, (c) $[(dY/dT) \cdot \phi / f(Y)] - 1/T$ curves for calculation slope Q , (d) Y-t curves of β'' phase fraction versus time.

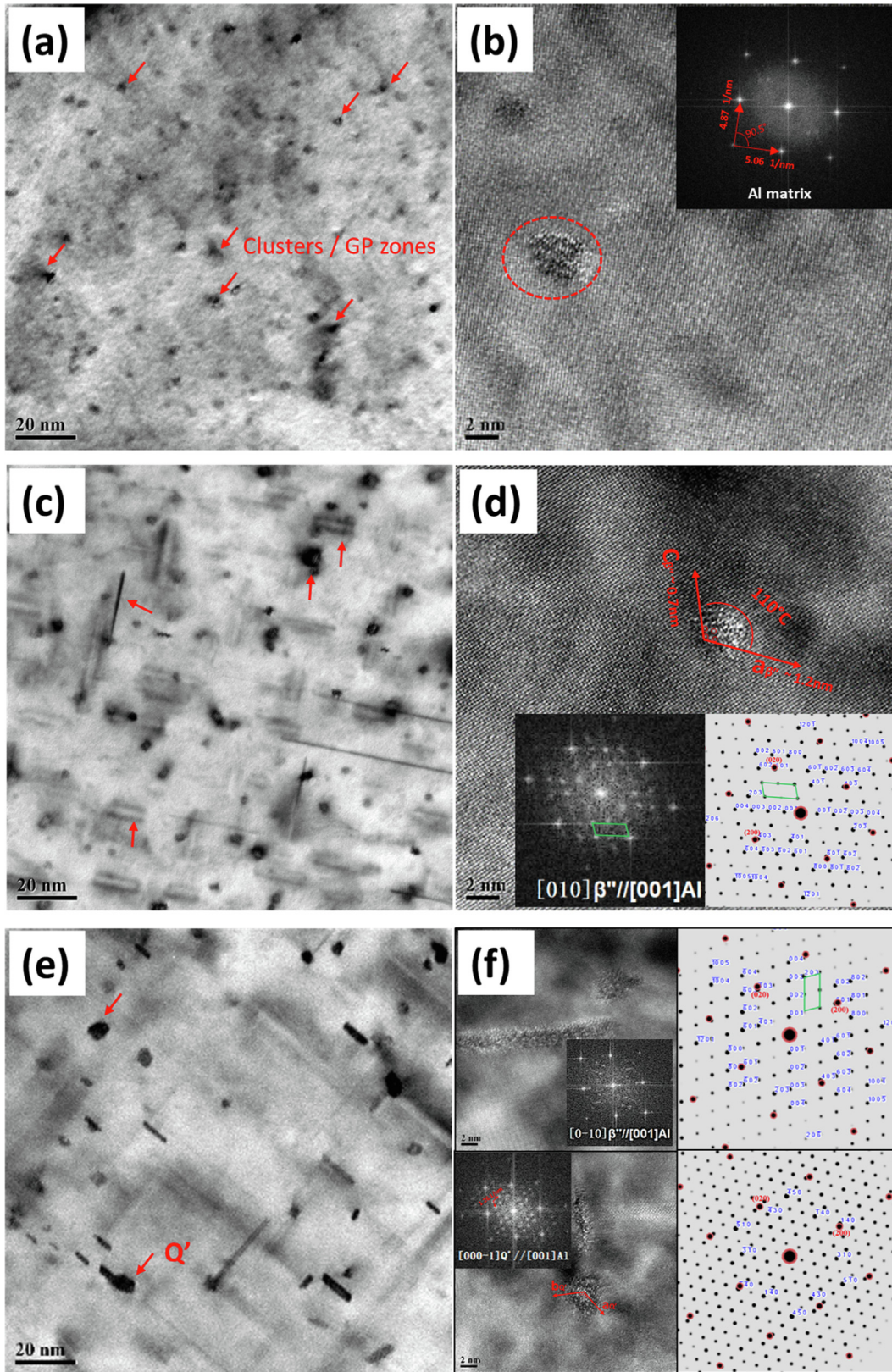


Fig. 8. TEM and HRTEM images with fast Fourier transform (FFT) and diffraction spot simulation of PA-0.2 samples after NA 0 day, pre-stained 2% and artificially aged at (a) (b) 185 °C for 20 min; (c)(d) 185 °C for 150 min; (e)(f) 185 °C for 20 h.

image quality of FFT spots, here we display simulated diffraction spots for each precipitate, based on the measurement results and standard crystal structures.

Fig. 8(a)(b) shows the sample in the underaged state. A large number of dot-like precipitates and small inconspicuous acicular precipitates appear in the matrix. These small dot-like precipitates

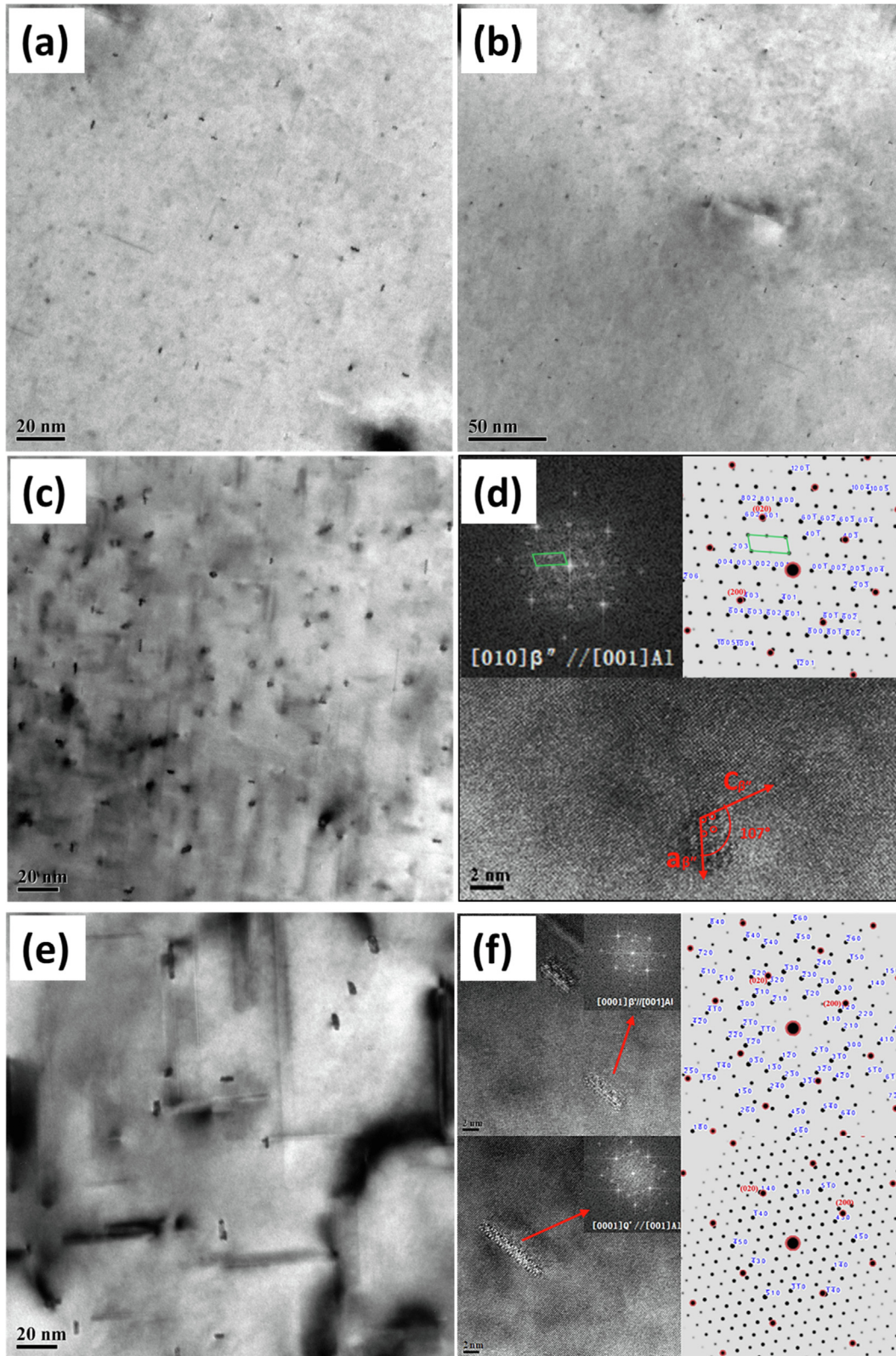


Fig. 9. TEM and HRTEM images with fast Fourier transform (FFT) and diffraction spot simulation of PA-0.2 samples after NA for 6 months, pre-strained with 2% and artificially aged at (a)(b) 185 °C for 20 min; (c)(d) 185 °C for 180 min; (e)(f) 185 °C for 20 h.

are GP zones with diameters of approximately 2 nm, but the distribution density is relatively high, which will provide nucleation sites for the rapid precipitation of the subsequent strengthening phase β'' . By performing fast Fourier transformation on the circled precipitate in the HRTEM image along the $[001]_{Al}$ direction, it is

found that except for diffraction spots of the Al matrix, no other precipitated phases are seen.

Fig. 8(c)(d) shows the sample in the peak-aged state. There are a large number of dot-like and needle-like precipitates that distribute perpendicularly to each other. The diameter of the dot-

like phase is slightly more than 2 nm, part of which is the cross section of the plug-in variant needle-like phase; others may be unknown precipitated phases or GP zones. The length of the acicular precipitates is approximately 20 nm, and they are distributed along the $[100]_{Al}$ and $[010]_{Al}$ directions. Meanwhile, an obvious coherent strain field can also be observed around the precipitates, i.e. the existence of a zero contrast line (shown by the black line in the figure) means that the alloy matrix basically consists of a coherent β'' phase along three $\langle 100 \rangle_{Al}$ directions. It is generally believed that the needle-shaped β'' phase is the main strengthening phase in Al-Mg-Si-Cu alloys because it is completely coherent with the matrix and can hinder the movement of dislocations, thereby significantly improving the strength of the alloy. Fig. 8(d) shows the peak-aged HRTEM structure and its FFT image with a diffraction spot simulation diagram. By comparing the experimental results and standard crystal structure simulation, certain orientations between β'' and the Al matrix are revealed. In the upper left corner, the FFT spots of needle-shaped β'' showing parallel relationship is: $[010]_{\beta''} // [001]_{Al}$, $(601)_{\beta''} // (200)_{Al}$, $(40-3)_{\beta''} // (020)_{Al}$; At the lower left corner, the FFT spots of cross section β'' showing parallel relationship is: $[010]_{\beta''} // [001]_{Al}$, $(-403)_{\beta''} // (200)_{Al}$, $(601)_{\beta''} // (020)_{Al}$.

Fig. 8(e)(f) shows the sample in the overaged state, and the precipitated phase in the matrix grows thicker and darker. The cross-section of the plug-in variant grows from dot-like to plate-like (rectangular) in shape, from 2 nm to 5 nm in diameter. The number of needle-like β'' phases decreased, and a rod-like phase with obvious contraction was formed. Phases with rod-like and plate-like morphologies are usually recognized as the β' phase and Q' phase, which contribute less hardness than the β'' phase, causing a hardness drop after peak aging. The HRTEM morphology and FFT analysis show that there is still some strengthening phase β'' that nucleates later in the over-aging state, but most of which grows into the β' and Q' phases. The upper left corner of Fig. 8(f) shows the inserted β' phase, and the orientation relationship with the matrix is $[0-10]_{\beta'} // [001]_{Al}$, $(601)_{\beta'} // (200)_{Al}$, and $(-403)_{\beta'} // (020)_{Al}$. The phase inserted into the matrix at the bottom left corner is the Q' phase, with an orientation relationship to the matrix of $[000-1]_{Q'} // [001]_{Al}$, $(14-50)_{Q'} // (200)_{Al}$, and $(-3210)_{Q'} // (020)_{Al}$. The lattice parameters of β'' phase measured from artificial aged samples in Fig. 8 are $a = 1.2$ nm, $c = 0.7$ nm, $\beta = 110^\circ$ in average, compared to that in [47], where the parameters are around 1.5 nm, 0.67 nm, and 106° respectively, the structure of β'' phase at peak aging state was slightly affected by the higher Zn content in studied alloys. The lattice parameter of Al matrix is 0.201 nm, which is lower than the standard pure Al of 0.286 nm.

Fig. 9 shows the TEM microstructure of PA-0.2 samples after NA 6 months, pre-deformed by 2%, and subjected to artificial aging at 185 °C. Compared with samples NA for 0 days, significant differences were found in the size, density and morphology of the precipitates.

Fig. 9(a)(b) shows a sample in the underaged state. The size and density of the precipitated spherical GP zone is much smaller than that shown in Fig. 8, which cannot be detected even at high resolution. This is because at the beginning stage of aging, the precipitates formed during the NA process are quickly redissolved into the matrix via channels induced by pre-strain, and few precipitated particles are observed.

When reaching the peak-aging state, as shown in Fig. 9(c)(d), the strengthening phase continues to precipitate and grow. Dot-like precipitates approximately 2 nm in diameter with high density are dominant, while needle-like precipitates are barely observed, which is the reason for the decrease in the peak age hardness value compared with the NA 0 day samples. Through FFT analysis, it is found that these precipitated phases are intercalated variants of β'' phases. The orientation relationship between the upper left cor-

ner β'' phase and the matrix is $[010]_{\beta''} // [001]_{Al}$, $(-403)_{\beta''} // (200)_{Al}$, $(601)_{\beta''} // (020)_{Al}$; the orientation relationship between the lower left corner inserted β'' phase and the matrix is $[0-10]_{\beta''}$, $(40-3)_{\beta''} // (200)_{Al}$, $(601)_{\beta''} // (020)_{Al}$.

After aging at 185 °C for 20 h, as shown in Fig. 9(e)(f), short needle-like precipitates were uniformly distributed in the matrix, with a length of only 4 nm. There are very few long needle-like precipitates. HRTEM analysis shows that the β'' phase transformed into the β' phase and Q' phase. The orientation relationship between the β' phase and matrix is, $(12-30)_{\beta'} // (200)_{Al}$, and $(-3210)_{\beta'} // (020)_{Al}$, while the orientation relationship between the Q' phase and the matrix is $[0001]_{Q'} // [001]_{Al}$, $(3-210)_{Q'} // (200)_{Al}$, and $(14-50)_{Q'} // (020)_{Al}$.

The lattice parameters of β'' phase measured from Fig. 9(d) has similar a and c values as in Fig. 8, but β is 107° , which is very close to the 106° in reference. The possible composition change of β'' phase couldn't be reflected by the measurements of lattice parameters after the natural aging process. However the minor difference can still be found when compared to Zn-free alloys[47,50].

Above all, TEM analysis reveals a significant difference between NA states and the following artificial aging states, specifically for the type, morphology and orientation of precipitates/phases. After 2% pre-strain, a large number of dislocations are induced into the alloy matrix. The alloy without natural aging does not contain significant precipitates, and Mg, Si, Zn atoms can quickly diffuse through the dislocation channel and promote nucleation, thereby accelerating the rapid precipitation of the strengthening phase. For alloys that have undergone long-term natural aging, as the natural aging time increases, the precipitated clusters and GP zones increase. Therefore, during the aging process at 185 °C, the clusters and GP zone redissolve first, the dislocations provide a fast diffusion channel for the redissolution of solute atomic clusters at the initial stage of aging at 185 °C, and the redieciation of the strengthening phase occurs only after redissolution to a certain extent. This is the main reason that the precipitated phases in Fig. 9 are less than those in Fig. 8 under the TEM view.

As the aging time increases, the strengthening phase β'' begins to precipitate and grow. After reaching the peak state, the coherent strengthening phase β'' transforms into the noncoherent β' phase and Q' phase, resulting in a decrease in hardness. The hardness curve and TEM analysis correspond well.

4. Discussion

4.1. Phase constituents and microstructure evolution in Al-Mg-Si-Cu-Zn alloys

The equilibrium condition was considered in the calculation, which provided a predicting tendency for precipitation evolution in the following sessions, i.e., the potential evolution pathway from the metastable state to the ideal stable state, the Scheil solidification model and phase property diagram are shown in Fig. 10.

Fig. 10(a) displays the Scheil solidification model in our alloy system, from which we can read the information of the nonequilibrium solidification process and the solid phase constituents versus temperature. The equilibrium line starts to significantly discretize from the solid line at approximately 620 °C, indicating that solute redistribution occurs. A new phase will form that is totally different from the previously formed solid phase, representing the formation of the α -Fe-rich phase. Following the α -Fe-rich phase, Mg_2Si , β -Fe-rich phase, $Al_3FeMg_3Si_6$ and Si particles are also subsequently precipitated, and Cu- and Zn-containing phases are not shown in the solidification results compared with the property diagram in Fig. 10(b), indicating that the solidification model mainly focuses on the solid-liquid interface and heterogeneous solutes,

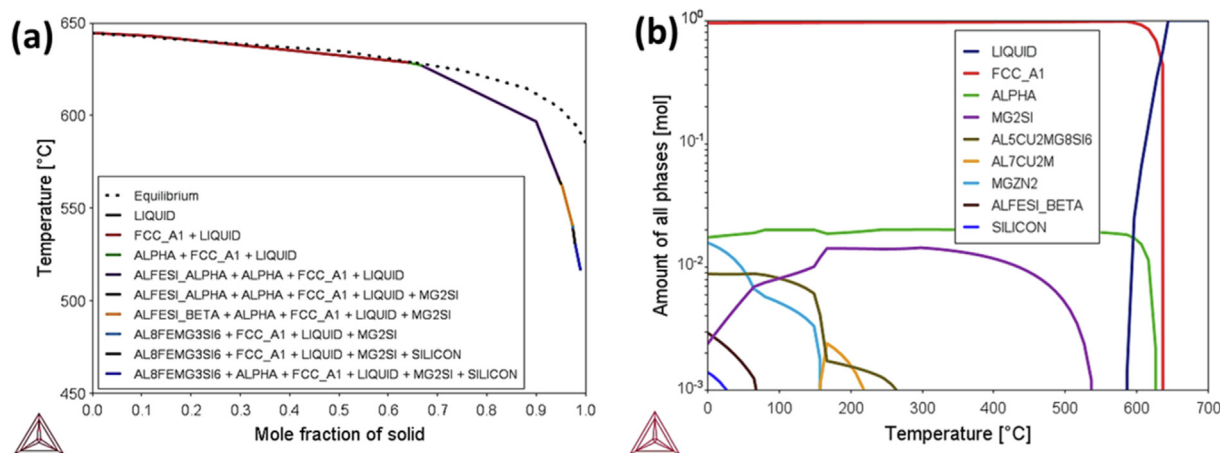


Fig. 10. Thermal calculation under equilibrium conditions: (a) Scheil solidification, (b) property diagram.

while Cu and Zn diffusion that occurs only in the solid-state will further change the phase constituents.

Combining both solidification and property diagrams, it can be concluded that Mg_2Si - and Fe-rich phases were first formed during solidification, with temperature cooling down, and Cu and Zn diffusion then occurred in the already formed solid phase. Zn tends to consume Mg atoms, forming the $MgZn_2$ phase and resulting in a reduction in the amount of Mg_2Si , as shown in Fig. 10(b). At approximately 160 °C, the purple line Mg_2Si decreases while the blue line $MgZn_2$ increases with temperature cooling down to room temperature. In addition, according to the phase property diagram, $MgZn_2$ would be the stable at room temperature, but will be completely dissolved at temperatures higher than 160 °C (for example artificial aging temperature 185 °C), which is important for subsequent precipitation analysis.

4.2. Precipitation behavior of GP zones

GP zones are fully coherent with the matrix, so we remove the stable phase FCC from the system during the calculation, and then the formation behavior of metastable GP zones can be evaluated. The formation temperature was 109.44 °C, and the fraction of GP zones at PA temperature and chemical compositions were also calculated, as shown in Fig. 11.

Fig. 11(a) shows that the precipitating fraction increased from the formation temperature to room temperature, and the formation rates can be read from the slope of the fraction lines. Since all three PA treatments were in the same temperature range, the fractions of GP zones were the same; specifically, the forming rates were also the same during the PA temperature range. Therefore, the change in PA cooling rates only changes the morphology and distribution of GP zones instead of volume fractions. Compared to isothermal or step cooling pre-aging that hold long time at specific temperature, the clusters and GP zones will continuously grow, accordingly lead to lower number density (then have less nucleate sites for strengthening phase at painting stage). According to the differential method, the PA treatments PA-0.2, PA-0.3, and PA-0.4 can be interpreted as holding 5 min, 3.3 min and 2.5 min per degree, respectively. Therefore, the slowest cooling rate allows more full solute diffusion during longer PA time, and larger and more stable GP zones can be obtained.

Fig. 11(b) displays the chemical composition of GP zones at temperatures within the PA range. Zn and Mg are dominant in GP zones, while Si is minimally contained, which is different from the traditional thinking of Mg-Si clusters in Al-Mg-Si alloys [10–14], but corresponds with the finding of Zn-containing precipitates mentioned in previous research [27]. During the metastable calcu-

lation process, the chemical composition changed slightly with cooling, and the ratio of Zn and Al gradually decreased; in contrast, the fraction of Mg and Cu increased. Considering that $MgZn_2$ and $Al_5Cu_2Mg_8Si_5$ are stable phase formats for Zn and Cu atoms from the property diagram in the last session, the chemical composition change with temperature can be seen as a stabilization process from meta-stable precipitates to a room temperature stable phase. However, before reaching the final stable phase, the clusters precipitation behavior will be also affected by the aging (natural or artificial) process.

Above all, a longer PA time was beneficial for the full diffusion of elements from precipitates to the stable phase. We can conclude that the slowest cooling rate of the PA-0.2 sample contains the most stable GP zones, while the PA-0.4 sample contains the least stable GP zones. This explained the hardness change in Fig. 2. A lower hardness value was observed in PA-0.4 immediately after PA treatment, corresponding to the less stable GP zones. Then, PA-0.2 and PA-0.3 samples rapidly joined the same tendency, indicating the similar phase formation. Specifically, the hardness of all three PA samples remained almost unchanged within the first 14 days, and excellent natural aging resistance was obtained by PA treatment and Zn-containing precipitates. Apparently, the existence of Mg-Zn- clusters is an obstacle for the formation of pure Mg-Si phase, which need more time to exclude Zn atoms while realize the aging stability.

DSC experimental results in Fig. 5, that samples after PA show an exothermic peak approximately 160–200 °C, according to above analysis, after PA treatment without NA process, Mg-Zn phases are still the dominant precipitates that would tend to form $MgZn_2$ structure, according to the Enthalpy calculation in Fig. 12(a), the exothermic peak must be dissolution of $MgZn_2$ structure and after then Mg-Si clusters can form and play the important role in following β'' phase formation. Fig. 12(b) reveals that Si is sensitive to temperature change, which is also the nature of phase precipitation in Al-Mg-Si alloys. Therefore, after long-term NA, Fig. 5 (b) did not have the exothermic peak of $MgZn_2$; instead, an exothermic peak at approximately 70–100 °C was observed, indicating that traditional Mg-Si clusters formed during the long NA process.

4.3. Effect of PA treatment on age-hardening behaviors

Fig. 13 illustrates the clustering process at different states; here, we display only the slowest PA-0.2 and fastest PA-0.4 cooling rates, and PA-0.3 can be considered to fall within this range. As described in the experimental results and discussed above, the clustering process can be divided into three main stages after PA treatment.

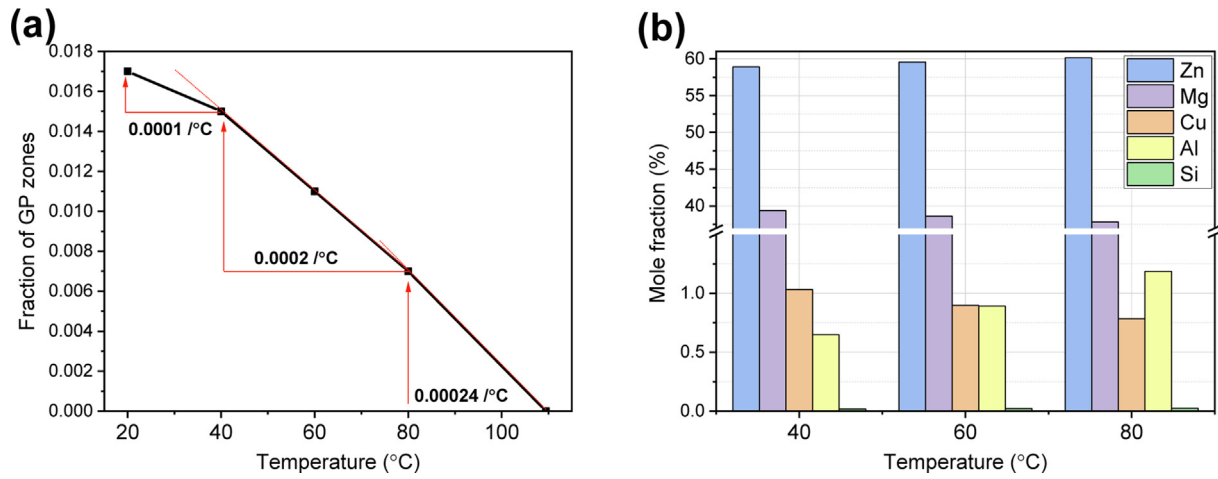


Fig. 11. Precipitation behavior evaluation of GP zones: (a) fraction of GP zones versus temperature, (b) chemical composition of GP zones versus temperature.

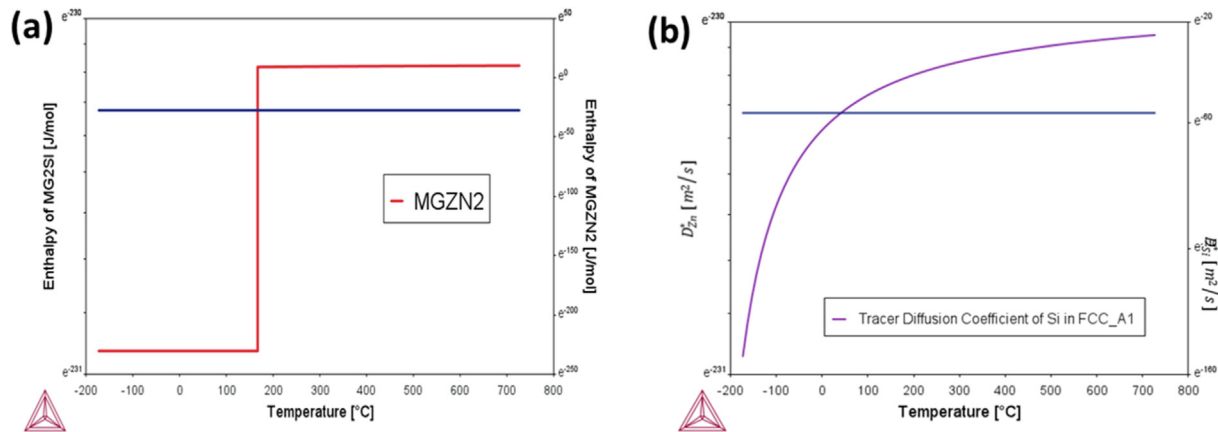


Fig. 12. The diffusion behaviour of Zn and Si versus temperature in our alloy system: (a) The standard molar enthalpy of Mg₂Si and MgZn₂, (b) The tracer diffusion coefficient of Zn and Si in the matrix.

Immediately after PA treatment, Mg-Zn clusters were the dominant precipitates at this stage. Due to the difference in PA time, the PA-0.2 sample has a longer time for solute clustering (precipitate growth) and accordingly has larger precipitates than that in the

PA-0.4 sample, which is expressed as a higher hardness value in Fig. 2. When performing DSC at this stage, Mg-Zn clusters will first redissolve to allow Si atoms to participate, and PA-0.2 and PA-0.4 will exhibit similar exothermic peaks and β'' activation energies

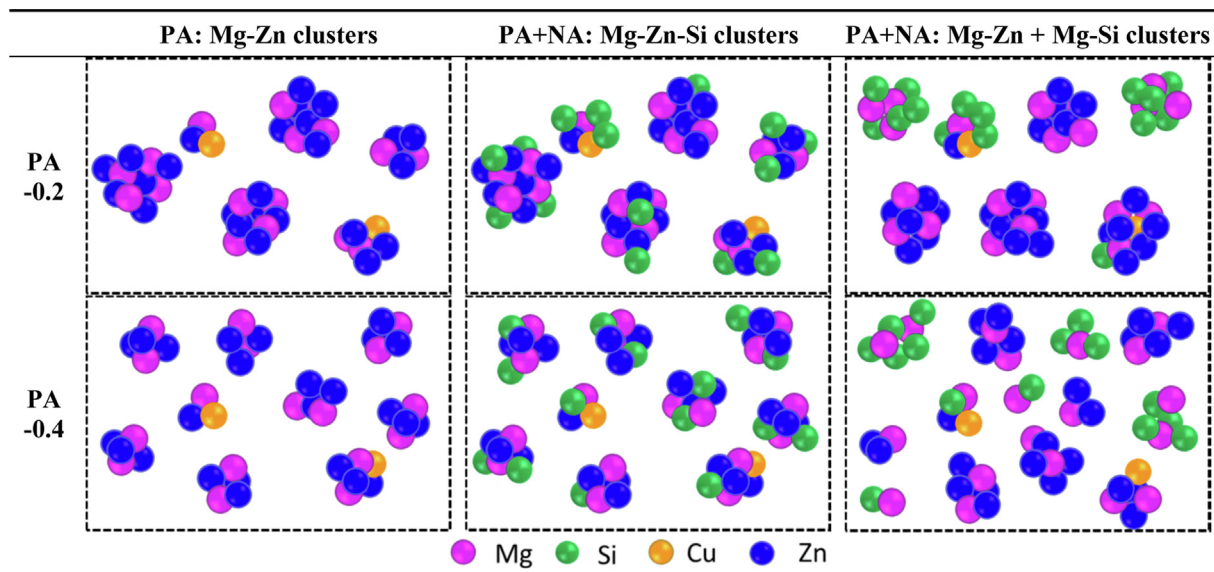


Fig. 13. Cluster evolution process at different states for alloys with different PA cooling rates.

because of the same fraction of GP zones after PA, which corresponds well with Fig. 5 and Table 3. When performing tensile tests at this stage, larger precipitates in PA-0.2 will cause a higher YS, small precipitates in PA-0.4 cause lower YS, and after paint baking, more nucleus sites in PA-0.4 will accelerate the formation of the strengthening phase, hence an extremely bake hardenability of 180 MPa was obtained, which corresponds with the data in Table 2, Fig. 3(a) and Fig. 4(a).

After PA samples were NA for some time, Si atoms gradually diffused and joined with Mg-Zn clusters, Mg-Zn clusters tended to form a stable Mg-Zn phase, but Si particles tended to capture Mg and form Mg-Si clusters (a further stable Mg_2Si phase). Since there is no in situ characterization of the clustering process, the Mg-Zn-Si clustering stage can be considered within NA 14 days, where the hardness value did not increase significantly, as shown in Fig. 2. Considering the smaller size of clusters in the PA-0.4 sample, more Mg atoms are exposed to the matrix and attract Si atoms than that in PA-0.2 sample, which deteriorates the formability by increasing the YS value faster.

When PA samples were NA for enough time, Mg-Si clusters (exothermic peak in Fig. 5(b)) and Mg-Zn clusters coexisted, and Mg-Zn-Si clusters were not dominant any more. More precipitates will form in PA-0.4 than in PA-0.2 due to the previous size advantage. NA 6 months can be seen at this stage, hardness keep increasing (Fig. 2), bake-hardening increment was lowered a lot (Table 2), strengthening phase β'' was much less than PA state (smaller peak area in Fig. 5(b) and Figs. 8, 9). After 6 months of NA, the PA-0.2 and PA-0.4 samples did not show significant differences in mechanical properties, although DSC proved slightly easier formation of the β'' phase in the PA-0.4 sample, which can be attributed to the smaller size of precipitates and more pre-existing Mg-Si clusters, as illustrated below.

5. Conclusions

- (1) The new pre-aging treatment with different cooling rates exhibits excellent natural aging stability and a bake-hardening response. The bake-hardening increment can reach 180 MPa, and the hardness remains unchanged for 14 days at a lower level of approximately 85 HV_{0.2}. Non-isothermal pre-aging on the one hand suppress the growth of GP/cluster/precipitates, contributing to lower hardness level; On the other hand provided enough small size precipitates, offering nuclei sites for strengthening phase easier formation.
- (2) The formation of GP zones during PA treatment was modelled and analysed, with a precipitation temperature of 109.44 °C and constitution of Mg_2Zn_3 . Zn is dominant in the GP zones of the studied Al-Mg-Si-Cu-Zn alloy. The pre-formed Mg-Zn clusters need extra time to dissolve before the formation of Mg-Si- clusters/phase, therefore enhancing the natural aging stability of alloys.
- (3) TEM characterization exhibits different types of phases formed at the corresponding aging state: the alloy matrix in the underaged state is dominated by clusters and GP zones, that in the peak-aged state is dominated by the β'' phase, and that in the overaged state is dominated by the β' and Q' phases, which all have certain orientations with the matrix. However, after 6 months of natural aging, there is a significant decrease in the size, density, and ratio of the strengthening phase, which also met the peak hardness value drop.
- (4) Activation energy of β'' phase is measured. DSC analysis shows that the precipitation energy of β'' is related to the cooling rate of the PA treatment. Within a specific tempera-

ture range, lower cooling rate allows precipitates to grow, resulting in less activation energy needed later. After long-term NA, nucleation sites are consumed by room temperature precipitation; hence, the advantage disappears.

- (5) The phase constituents and microstructure were understood, and the clustering process and ageing behaviour over a long time scope were illustrated and explained.

Declaration of Competing Interest

The authors declare that they have no known competing financial interests or personal relationships that could have appeared to influence the work reported in this paper.

Acknowledgements

This work was supported by the National Key Research and Development Program of China (No.2021YFE0115900), the National Natural Science Foundation of China (No.51871029, No.51571023 and No.51301016), Government Guided Program-Intergovernmental Bilateral Innovation Cooperation Project (No. BZ2019019), the Opening Project of State Key Laboratory for Advanced Metals and Materials (No. 2020-ZD02) and Industry-University Cooperation Collaborative Education Project (Nos. 202102437001, 202102437002).

References

- [1] W.S. Miller, L. Zhuang, J. Bottema, A.J. Wittebrood, P. De Smet, A. Haszler, A. Viergege, Recent development in aluminium alloys for the automotive industry, *Mater. Sci. Eng., A* 280 (1) (2000) 37–49.
- [2] M. Murayama, K. Hono, Pre-precipitate clusters and precipitation processes in Al-Mg-Si alloys, *Acta Mater.* 47 (1999) 1537–1548, [https://doi.org/10.1016/S1359-6454\(99\)00033-6](https://doi.org/10.1016/S1359-6454(99)00033-6).
- [3] C. Ravi, C. Wolverton, First-principles study of crystal structure and stability of Al-Mg-Si-(Cu) precipitates, *Acta Mater.* 52 (2004) 4213–4227, <https://doi.org/10.1016/j.actamat.2004.05.037>.
- [4] A.K. Gupta, D.J. Lloyd, S.A. Court, Precipitation hardening in Al-Mg-Si alloys with and without excess Si, *Mater. Sci. Eng., A* 316 (2001) 11–17, [https://doi.org/10.1016/S0921-5093\(01\)01247-3](https://doi.org/10.1016/S0921-5093(01)01247-3).
- [5] R.K.W. Marceau, A. de Vaucorbeil, G. Sha, S.P. Ringer, W.J. Poole, Analysis of strengthening in AA6111 during the early stages of aging: Atom probe tomography and yield stress modelling, *Acta Mater.* 61 (19) (2013) 7285–7303.
- [6] L. Zhang, K.e. Li, H. He, L.-X. Li, Influence of prolonged natural aging followed by artificial aging on tensile properties and compressive behavior of a thin-walled 6005 aluminum alloy tube, *Journal of Central South University* 28 (9) (2021) 2647–2659.
- [7] G.A. Edwards, K. Stiller, G.L. Dunlop, M.J. Couper, The precipitation sequence in Al-Mg-Si alloys, *Acta Mater.* 46 (11) (1998) 3893–3904.
- [8] S.J. Andersen, C.D. Marioara, J. Friis, R. Holmestad, Precipitates in aluminium alloys, *Advances in Physics*: X 3 (1) (2018) 1479984.
- [9] D.W. Pashley, M.H. Jacobs, J.T. Vietz, The basic processes affecting two-step ageing in an Al-Mg-Si alloy, *Phil. Mag.* 16 (1967) 51–76, <https://doi.org/10.1080/14786436708229257>.
- [10] L.Z. He, H.T. Zhang, J.Z. Cui, Effects of Pre-Ageing Treatment on Subsequent Artificial Ageing Characteristics of an Al-1.01Mg-0.68Si-1.78Cu Alloy, *J. Mater. Sci. Technol.* 26 (2010) 141–145, [https://doi.org/10.1016/S1005-0302\(10\)60023-0](https://doi.org/10.1016/S1005-0302(10)60023-0).
- [11] C.H. Shen, Pre-treatment to Improve the Bake-hardening Response in the Naturally Aged Al-Mg-Si Alloy, *J. Mater. Sci. Technol.* 27 (2011) 205–212, [https://doi.org/10.1016/S1005-0302\(11\)60050-9](https://doi.org/10.1016/S1005-0302(11)60050-9).
- [12] H.C. Liao, Y.N. Wu, K. Ding, Hardening response and precipitation behavior of Al-7%Si-0.3%Mg alloy in a pre-aging process, *Mater. Sci. Eng., A* 560 (2013) 811–816, <https://doi.org/10.1016/j.msea.2012.10.041>.
- [13] L. Yan, Z. Li, Y.-a. Zhang, B. Xiong, X. Li, H. Liu, S. Huang, H. Yan, Pre-aging on early-age behavior and bake hardening response of an Al-0.90Mg-0.80Si-0.64Zn-0.23Cu alloy, *Progress in Natural Science: Materials International* 26 (4) (2016) 398–403.
- [14] S. Jin, T. Ngai, L. Li, Y. Lai, Z. Chen, A. Wang, Influence of natural aging and pre-treatment on the precipitation and age-hardening behavior of Al-1.0Mg-0.65Si-0.24Cu alloy, *J. Alloy. Compd.* 742 (2018) 852–859.
- [15] S.Q. Zhu, H.C. Shih, X.Y. Cui, et al., Design of solute clustering during thermomechanical processing of AA6016 Al-Mg-Si alloy, *Acta Materialia* 203 (2021), <https://doi.org/10.1016/j.actamat.2020.10.074>.

- [16] P. Castany, F. Diologent, A. Rossoll, J.-F. Despois, C. Bezençon, A. Mortensen, Influence of quench rate and microstructure on bendability of AA6016 aluminum alloys, *Mater. Sci. Eng., A* 559 (2013) 558–565.
- [17] K. Matsuda, S. Ikeno, Y. Uetani, et al., Metastable Phases in an Al-Mg-Si Alloy Containing Copper, *Metall. Mater. Trans. A* 32 (2001) 1293–1299. <https://link.springer.com/article/10.1007%2Fs11661-001-0219-2/metrics>.
- [18] A.A. Vasilyev, A.S. Gruzdev, N.L. Kuz'min, Calculation of the Solvus Temperature of Metastable Phases in the Al-Mg-Si Alloys, *Phys. Solid State* 53 (2011) 1902–1908. <https://doi.org/10.1134/S1063783411090320>.
- [19] A.A. Vasilyev, N.L. Kuzmin, A.S. Gruzdev, Study of the Formation Kinetics of Metastable Phases in Quenched Al-Mg-Si Alloys, *Phys. Solid State* 53 (2011) 1658–1663. <https://doi.org/10.1134/S1063783411080324>.
- [20] Y. Hu, W.A. Curtin, Modeling peak-aged precipitate strengthening in Al-Mg-Si alloys, *J. Mech. Phys. Solids* 151 (2021). <https://doi.org/10.1016/j.jmps.2021.104378>
- [21] H. Miyoshi, H. Kimizuka, A. Ishii, S. Ogata, Temperature-dependent nucleation kinetics of Guinier-Preston zones in Al-Cu alloys: An atomistic kinetic Monte Carlo and classical nucleation theory approach, *Acta Mater.* 179 (2019) 262–272.
- [22] H. Miyoshi, H. Kimizuka, A. Ishii, et al., Competing nucleation of single- and double-layer Guinier-Preston zones in Al-Cu alloys, *Sci. Rep.* 11 (2021) 4503. <https://doi.org/10.1038/s41598-021-83920-8>.
- [23] X.L. Chen, C.D. Marioara, S.J. Andersen, et al., Precipitation processes and structural evolutions of various GPB zones and two types of S phases in a cold-rolled Al-Mg-Cu alloy, *Materials and Design* 199 (2021). <https://doi.org/10.1016/j.matdes.2020.109425>.
- [24] X.L. Chen, C.D. Marioara, S.J. Andersen, et al., Data on atomic structures of precipitates in an Al-Mg-Cu alloy studied by high resolution transmission electron microscopy and first-principles calculations, *Data in Brief* 34 (2021). <https://doi.org/10.1016/j.dib.2021.106748>.
- [25] N.N. Jiao, Y.X. Lai, S.L. Chen, P. Gao, J.H. Chen, Atomic-scale roles of Zn element in age-hardened AlMgSiZn alloys, *J. Mater. Sci. Technol.* 70 (2021) 105–112.
- [26] F. Glöckel, P.J. Uggowitzer, P. Felfer, S. Pogatscher, H.W. Höppel, Influence of Zn and Sn on the precipitation behavior of new Al-Mg-Si alloys, *Materials* 12 (16) (2019) 2547.
- [27] M.X. Guo, J.Q. Du, C.H. Zheng, J.S. Zhang, L.Z. Zhuang, Influence of Zn contents on precipitation and corrosion of Al-Mg-Si-Cu-Zn alloys for automotive applications, *J. Alloy. Compd.* 778 (2019) 256–270.
- [28] M.X. Guo, G.J. Li, Y.D. Zhang, G. Sha, J.S. Zhang, L.Z. Zhuang, E.J. Lavernia, Influence of Zn on the distribution and composition of heterogeneous solute-rich features in peak aged Al-Mg-Si-Cu alloys, *Scr. Mater.* 159 (2019) 5–8.
- [29] Y. Pazhuhfar, B. Eghbali, Processing and characterization of the microstructure and mechanical properties of Al6061-TiB₂ composite, *Int. J. Miner. Metall. Mater.* 28 (2021) 1080–1089. <https://doi.org/10.1007/s12613-021-2288-0>.
- [30] X.-F. Wang, M.-X. Guo, W.-F. Peng, Y.-G. Wang, L.-Z. Zhuang, Relationship among solution heating rate, mechanical properties, microstructure and texture of Al-Mg-Si-Cu alloy, *Trans. Nonferrous Metals Soc. China* 31 (1) (2021) 36–52.
- [31] Y. Wang, Y.L. Deng, Q.S. Dai, et al., Microstructures and strengthening mechanisms of high Fe containing Al-Mg-Si-Mn-Fe alloys with Mg, Si and Mn modified, *Mater. Sci. Eng., A* 803 (2021). <https://doi.org/10.1016/j.msea.2020.140477>.
- [32] H. Ebrahimzadeh, H. Farhangi, S.A.A.A. Mousavi, A. Ghahramani, Microstructural analyses of aluminum-magnesium-silicon alloys welded by pulsed Nd: YAG laser welding, *Int. J. Miner. Metall. Mater.* 27 (5) (2020) 660–668.
- [33] Q.J. Zheng, J. Wu, H.X. Jiang, et al., Effect of micro-alloying element La on corrosion behavior of Al-Mg-Si alloys, *Corrosion Science* 179 (2021). <https://doi.org/10.1016/j.corsci.2020.109113>.
- [34] X.-K. Yang, B.-Q. Xiong, X.-w. Li, L.-Z. Yan, Z.-H. Li, Y.-a. Zhang, Y.-N. Li, K. Wen, H.-W. Liu, Effect of Li addition on mechanical properties and ageing precipitation behavior of extruded Al-3.0Mg-0.5Si alloy, *J. Central South University* 28 (9) (2021) 2636–2646.
- [35] M.X. Guo, Y.D. Zhang, G.J. Li, S.B. Jin, G. Sha, J.S. Zhang, L.Z. Zhuang, E.J. Lavernia, Solute clustering in Al-Mg-Si-Cu-(Zn) alloys during aging, *J. Alloy. Compd.* 774 (2019) 347–363.
- [36] M.X. Guo, G. Sha, L.Y. Cao, W.Q. Liu, J.S. Zhang, L.Z. Zhuang, Enhanced bake-hardening response of an Al-Mg-Si-Cu alloy with Zn addition, *Mater. Chem. Phys.* 162 (2015) 15–19.
- [37] R. Prillhofer, G. Rank, J. Berneder, H. Antrekowitsch, P. Uggowitzer, S. Pogatscher, Property criteria for automotive Al-Mg-Si sheet alloys, *Materials* 7 (7) (2014) 5047–5068.
- [38] O. Engler, C. Schäfer, H.-J. Brinkman, J. Brecht, P. Beiter, K. Nijhof, Flexible rolling of aluminium alloy sheet—process optimization and control of materials properties, *J. Mater. Process. Technol.* 229 (2016) 139–148.
- [39] Y. Birol, Effect of natural ageing on the performance of pre-ageing to improve bake-hardening response of a twin-roll cast Al-Mg-Si alloy, *Zeitschrift für Metallkunde* 96 (2005) 380–384. <https://doi.org/10.3139/146.018123>.
- [40] Y. Birol, Restoration of the bake hardening response in a naturally aged twin-roll cast AlMgSi automotive sheet, *Scr. Mater.* 54 (2006) 2003–2008. <https://doi.org/10.1016/j.scriptamat.2006.03.022>.
- [41] G.-J. Gao, C. He, Y. Li, J.-D. Li, Z.-D. Wang, R.D.K. Misra, Influence of different solution methods on microstructure, precipitation behavior and mechanical properties of Al-Mg-Si alloy, *Trans. Nonferrous Metals Soc. China* 28 (5) (2018) 839–847.
- [42] G.C. Ju, Y.S. Lee, M.S. Kim, et al., Bake-hardening properties of Al-0.6Mg-1.2Si alloy sheets fabricated by twin roll casting, *Korean Journal of Met. Mater.* 55 (2017) 853–861. <https://doi.org/10.3365/KJMM.2017.55.12.853>.
- [43] G. Lu, S. Nie, J. Wang, Y. Zhang, T. Wu, Y. Liu, C. Liu, Enhancing the bake-hardening responses of a pre-aged Al-Mg-Si alloy by trace Sn additions, *J. Mater. Sci. Technol.* 40 (2020) 107–112.
- [44] Q. Lu, K. Li, H. Chen, M. Yang, X. Lan, T. Yang, S. Liu, M. Song, L. Cao, Y. Du, Simultaneously enhanced strength and ductility of 6xxx Al alloys via manipulating meso-scale and nano-scale structures guided with phase equilibrium, *J. Mater. Sci. Technol.* 41 (2020) 139–148.
- [45] O. Engler, C.D. Marioara, Y. Aruga, M. Kozuka, O.R. Myhr, Effect of natural ageing or pre-ageing on the evolution of precipitate structure and strength during age hardening of Al-Mg-Si alloy AA 6016, *Mater. Sci. Eng., A* 759 (2019) 520–529.
- [46] S. Kleiner, P. Uggowitzer, C. Henkel, et al. Paint bake response of aluminium alloy 6016. *Aluminium: international journal for industry, research and application*, 77 (2001)185–189. https://www.researchgate.net/publication/318960774_Paint_bake_response_of_aluminium_alloy_6016.
- [47] B.o. Yuan, G. Li, M. Guo, L. Zhuang, Fast age-hardening response of Al-Mg-Si-Cu-Zn-Fe-Mn alloy via coupling control of quenching rate and pre-aging, *J. Mater. Res. Technol.* 14 (2021) 1518–1531.
- [48] C.-S. Tsao, C.-Y. Chen, U.-S. Jeng, T.-Y. Kuo, Precipitation kinetics and transformation of metastable phases in Al-Mg-Si alloys, *Acta Mater.* 54 (17) (2006) 4621–4631.
- [49] S. Esmaeili, D.J. Lloyd, Characterization of the evolution of the volume fraction of precipitates in aged AlMgSiCu alloys using DSC technique, *Mater. Charact.* 55 (2005) 307–319. <https://doi.org/10.1016/j.matchar.2005.07.007>.
- [50] B. Yuan, M.X. Guo, Y. Wu, et al., Influence of treatment pathways on the precipitation behaviors of Al-Mg-Si-Cu-(Zn)-Mn alloys, *J. Alloys Compounds* 797 (2019) 26–38. <https://doi.org/10.1016/j.jallcom.2019.05.055>.